Finding Good Configurations of Planar Primitives in Unorganized Point Clouds
-
Supplementary Material

Mulin Yu Florent Lafarge
Inria - Université Côte d'Azur

This supplementary material presents additional experiments with (i) visual results of planar primitive fitting from a variety of input point clouds, (ii) an example of object approximation at different levels of details, (iii) qualitative and quantitative comparisons with seven compact mesh reconstruction methods on the KSR42 dataset [1] and (iv) quantitative results with different fidelity metrics.

1. Additional visual results

Figure 1 shows results from a variety of input point clouds that differ in terms of (i) objects with buildings, mechanical pieces, furniture elements, statues and vehicles, and (ii) acquisition sensors with MVS-based point clouds, laser scans and points sampled from CAD models.

2. Reconstruction at different levels of details

Figure 2 shows an example of a freeform object reconstruction at different levels of details obtained by modifying the fitting parameters (ϵ, σ). Increasing progressively both the fitting tolerance ϵ and the minimal primitive size σ gives coarser configurations of planar primitives, and after assembling, more concise polygon meshes. Tables 1 and 2 provide the values of parameters ϵ and σ used for producing the results presented in the paper and this supplementary material.

3. Comparisons with compact mesh reconstruction methods

We compared our algorithm with seven compact mesh reconstruction methods on the KSR42 dataset by following the evaluation protocol of [1]. In particular, we considered as evaluation metrics the symmetric mean Hausdorff distance between input points and output mesh, the mean Hausdorff distance from input points to output mesh and the mesh simplicity given by the number of polygonal facets.

The seven methods include three compact mesh reconstruction methods (Polyfit [6], Chauve's algorithm [2] and KSR [1]) and four surface approximation pipelines where a dense mesh is first reconstructed from input points by the Screened Poisson algorithm before being simplified either by the edge collapse method QEM [4], by variational shape approximation VSA [3], by plane-guided mesh decimation SAMD [9] or by an alternative of the latter with corner preservation SAMD-CP. The Screened Poisson algorithm was used with an octree depth set to 9.

Tables 5 and 6 provide quantitative results on respectively the simple and advanced models of the KSR42 dataset. Our algorithm outperforms the other methods on both the accuracy and the mesh simplicity in most of simple and advanced models. On a few models such as *Building C*, the KSR algorithm performs better: it typically corresponds to regular scenes where the planar primitives detected by Region Growing have been consolidated according to parallelism and orthogonality regularities before assembling. Such geometric prior offers an advantage to KSR on such particular scenes by reducing the number of detected planar primitives. Yet, our algorithm gives better results on a large majority of models, showing that our primitive detection algorithm is more efficient than the traditional Region Growing used by the KSR algorithm. Figures 3, 4, 5 and 6 show visual comparisons on the simple models. Similarly, Figures 7, 8, 9 and 10 focus on advanced models. Note that Polyfit [6] and Chauve's algorithm [2] do not scale well enough to produce results on advanced models.

4. Choice of the fidelity metric

While fidelity is measured through the traditional Euclidean distance from point to plane in the paper, other metrics can be considered. Normal deviation can be an option when input normals are available or can be accurately estimated. Tables 3 and 4, which are an enriched version of Tab.1 and 2 of the paper, show quantitative results from two fidelity metrics: the traditional Euclidean distance used in the paper and the normal deviation. They are used as both evaluation score and metric in the energy (i.e. in Eq.2 of the paper). As expected, fidelity score is lower when computed with the same metric in the energy. However, the other fi-

delity score remains competitive with respect to the values from existing methods.

Model	$\#pts$	σ (%)	$diag$	ϵ
Sphere (Fig.1)	100K	0.2	3.5	0.008
Torus (Fig.3)	146K	0.034	11.5	0.04
Barn (Fig.5)	619K	0.048	8.9	0.04
Meeting room (Fig.5)	3M	0.003	22.9	0.02
Wave (Fig.7)	2.9M	0.003	222.6	0.20
Trex-Skul (Fig.7)	788K	0.012	194	0.20
Indoor Scene (Fig.7)	5M	0.006	187.8	0.40
Sappho head (Fig.7)	1.5M	0.003	129.5	0.40
Family (Fig.7)	1.1M	0.002	3.9	0.016
Urban (Fig.7)	4.6M	0.005	968.7	0.50
Torus (Fig.8)	146K	0.034	11.5	0.03
Eraser ball (Fig.8)	728K	0.021	3.0	0.005
Bunny (Fig.8)	146K	0.034	0.25	0.001
Lamp (Fig.9)	290K	0.017	1.0	0.001
Airplane (Fig.9)	731K	0.007	1.0	0.002
Table (Fig.9)	737K	0.007	1.0	0.004
Chair (Fig.9)	293K	0.010	1.0	0.004

Table 1. Parameters (ϵ, σ) used for producing the results illustrated in the paper. The size of input points ($\#pts$) ranges from 100K to 5M. The minimal primitive size σ is expressed in percent of $\#pts$. The fitting tolerance ϵ is expressed in the unit system of the input point clouds. $diag$ refers to the length of the bounding box diagonal of the input point clouds.

Model	$\#pts$	σ (%)	$diag$	ϵ
Francis statue	2.0M	0.01	6.6	0.05
curved Hilbert cube	1.0M	0.005	51.9	0.21
Earth globe	1.4M	0.004	93.6	0.20
House triplet	900K	0.011	67.9	0.12
Engine	1.5M	0.001	207.9	0.10
Observatory	246K	0.008	116.5	0.80
Vase	731K	0.007	115.8	0.90
Carter	193K	0.026	165.2	0.66
Owl statue	1.5M	0.001	182.3	0.07
M-W building	3.0M	0.005	67.5	0.35
Train	1.5M	0.010	11.4	0.005
Building Blocks	1.5M	0.013	210.5	0.90
Mechanical system	1.1M	0.005	303.1	1.00
basic House	868K	0.046	32.7	0.20
Chair	204K	0.010	749.4	3.50
large House	2.6M	0.008	46.7	0.30

Table 2. Parameters (ϵ, σ) used for producing the results illustrated in Figure 1 of this supplementary material.

		Fid. L_2	Fid. normal	Compl.	Simpl.
KSR	RG [8]	0.39	13.8	83.6	654.2
	SRG [7]	0.43	13.8	83.9	612.7
	RANSAC [10]	0.42	16.7	83.3	684.7
	Ours-L_2	**0.33**	13.3	84.1	572.4
	Ours-$normal$	0.4	**12.8**	**84.2**	**504.8**
ABC	RG [8]	0.28	10.3	97.6	69
	SRG [7]	0.30	10.6	97.1	65
	RANSAC [10]	0.21	10.6	97.7	55.5
	Ours-L_2	**0.19**	11.8	**97.9**	**39.4**
	Ours-$normal$	0.27	**9.9**	**97.9**	41.6

Table 3. Comparison with traditional methods using two different fidelity metrics. The table is an enriched version of Tab.1 of the paper with an average normal deviation score (Fid. normal, in degree) and with a variant of our algorithm using a normal deviation based metric (Ours-$normal$).

		Fid. L_2	Fid. normal	Compl.	Simpl.
ABC*	SPFN [5]	2.835	29.7	90.0	12.2
	ParSeNet [11]	0.410	10.9	99.1	8.8
	HPNet [12]	0.224	8.9	96.8	**8.3**
	Ours-L_2	0.130	4.4	99.8	**8.3**
	Ours-$normal$	**0.026**	**1.6**	**99.9**	8.8
ANSI*	SPFN [5]	0.760	20.1	95.5	12.1
	ParSeNet [11]	1.064	31.8	91.0	**9.0**
	HPNet [12]	0.087	9.9	83.0	13.3
	Ours-L_2	**0.085**	7.7	95.5	9.7
	Ours-$normal$	0.097	**6.3**	**99.2**	12.1

Table 4. Comparison with deep learning methods using two different fidelity metrics. The table is an enriched version of Tab.2 of the paper with an average normal deviation score (Fid. normal, in degree) and with a variant of our algorithm using a normal deviation based metric (Ours-$normal$).

References

[1] Jean-Philippe Bauchet and Florent Lafarge. Kinetic shape reconstruction. *Trans. on Graphics*, 39(5), 2020. 1

[2] Anne-Laure Chauve, Patrick Labatut, and Jean-Philippe Pons. Robust piecewise-planar 3D reconstruction and completion from large-scale unstructured point data. In *CVPR*, 2010. 1, 6

[3] David Cohen-Steiner, Pierre Alliez, and Mathieu Desbrun. Variational shape approximation. In *SIGGRAPH*, 2004. 1

[4] Michael Garland and Paul S. Heckbert. Surface simplification using quadric error metrics. In *SIGGRAPH*, 1997. 1

[5] Lingxiao Li, Minhyuk Sung, Anastasia Dubrovina, Li Yi, and Leonidas J Guibas. Supervised fitting of geometric primitives to 3d point clouds. In *CVPR*, 2019. 2

[6] Liangliang Nan and Peter Wonka. Polyfit: Polygonal surface reconstruction from point clouds. In *ICCV*, 2017. 1, 6

[7] Sven Oesau, Yannick Verdie, Clément Jamin, Pierre Alliez, Florent Lafarge, Simon Giraudot, Thien Hoang, and Dmitry Anisimov. Point set shape detection. In *CGAL User and Reference Manual*. 5.3 edition, 2021. 2

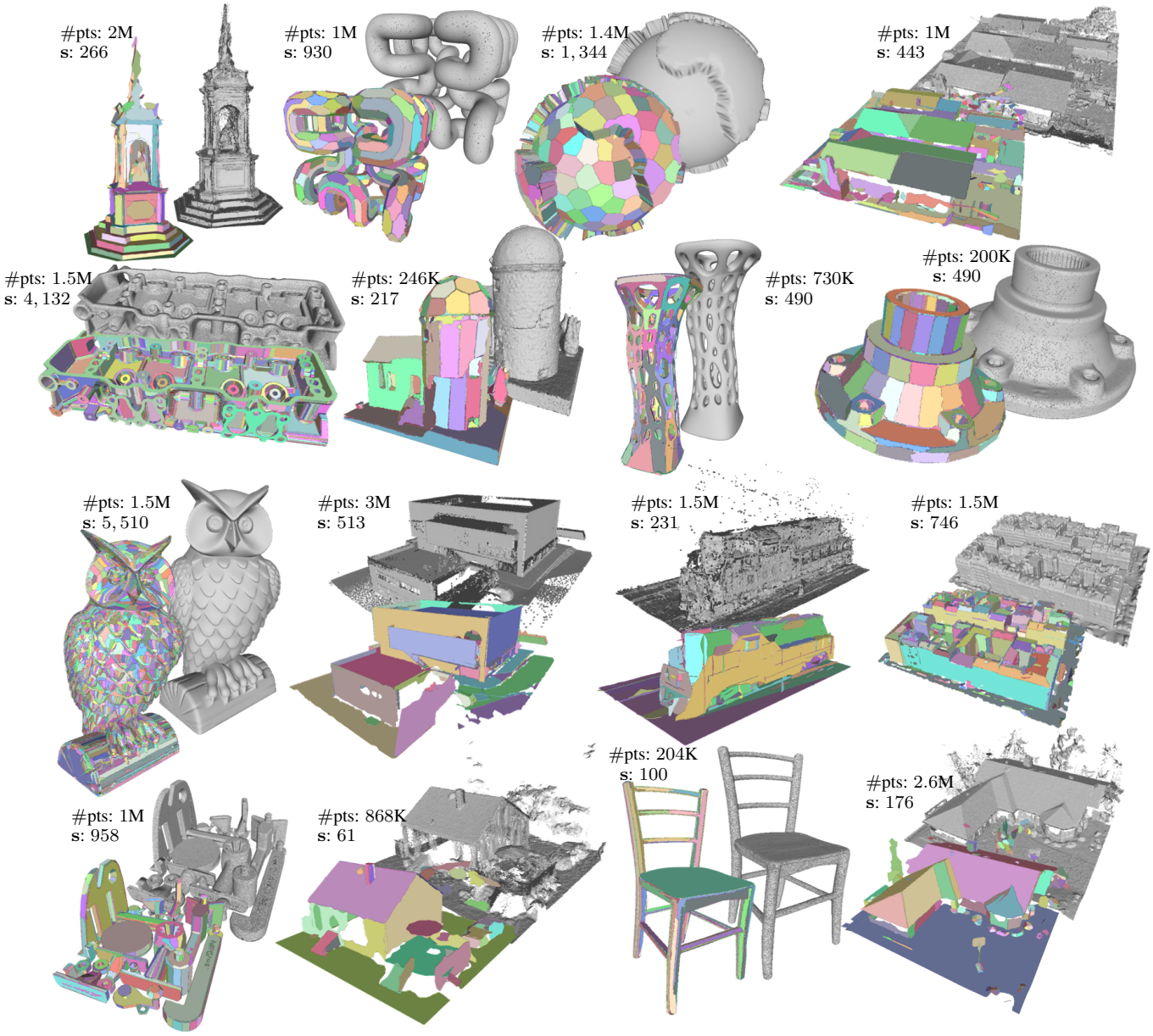

Figure 1. Visual results on a variety of input point clouds. From left to right, and top to bottom: Francis statue (MVS), curved Hilbert cube (CAD-based), Earth globe (CAD-based), residential House triplet (MVS), Engine (Laser), Observatory (MVS), Vase (Laser), Carter (Laser), Owl statue (Laser), Manhattan-World building (Laser), Train (MVS), Building Blocks (MVS), Mechanical system (CAD-based), basic House (MVS), Chair (Laser) and large House (MVS). #pts and s refer to the number of input points and the number of detected primitives respectively.

[8] Tahir Rabbani, Frank Van Den Heuvel, and George Vosselmann. Segmentation of point clouds using smoothness constraint. *International archives of photogrammetry, remote sensing and spatial information sciences*, 36(5), 2006. 2

[9] David Salinas, Florent Lafarge, and Pierre Alliez. Structure-Aware Mesh Decimation. *Computer Graphics Forum*, 34(6), 2015. 1

[10] Ruwen Schnabel, Roland Wahl, and Reinhard Klein. Efficient ransac for point-cloud shape detection. *Computer graphics forum*, 26(2), 2007. 2

[11] Gopal Sharma, Difan Liu, Subhransu Maji, Evangelos Kalogerakis, Chaudhuri, and Radomyr Mech. Parsenet: A parametric surface fitting network for 3d point clouds. In *ECCV*, 2020. 2

[12] Siming Yan, Zhenpei Yang, Chongyang Ma, Haibin Huang, Etienne Vouga, and Qixing Huang. Hpnet: Deep primitive segmentation using hybrid representations. In *ICCV*. 2

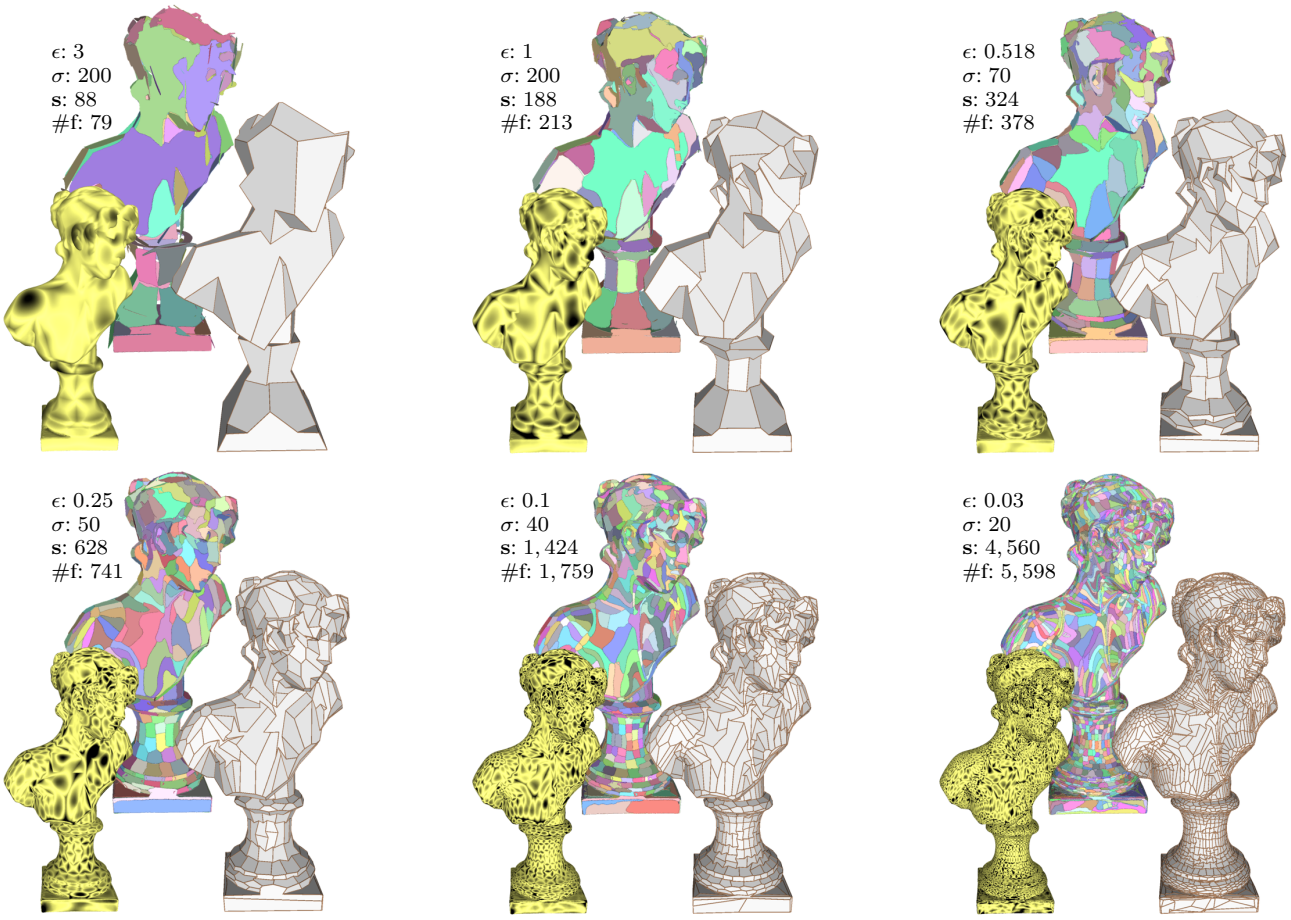

Figure 2. Reconstruction of a freeform object at different levels of details. By progressively decreasing the fitting parameters (ϵ, σ), our algorithm outputs a series of more and more accurate and complex planar primitive configurations (colored polygons, from left to right, and top to bottom). When combined with a plane assembly method, it produces polygon meshes at different levels details. $\mathbf{s}$ and #f refer to the number of primitives and the number of polygonal facets of the reconstructed mesh respectively. The colored point clouds show the distribution of the Hausdorff distance of input points to output mesh normalized by ϵ (yellow=0, black$\geq \epsilon$).

		Barn MVS	Building A	Building B	Building C	Bunny	Chair	Cottage	Couch	Fertility-Coarse	Foam box	Hand	Lans-Coarse	Rocker arm	Rooms A	Rooms B	Temple
Type		U	U	U	U	F	S	U	S	F	S	F	U	S	I	I	S
Origin		MVS	MVS	MVS	MVS	Laser	Laser	MVS	Laser	Laser	Laser	Laser	Laser	Laser	Laser	Laser	MVS
# pts		619K	101K	73K	577K	146K	756K	143K	911K	242K	382K	369K	1.22M	733K	186K	176K	621K
ϵ		0.75	5	2.5	0.4	0.4	1.6	0.7	2.2	1.75	1.75	0.8	1	1.1	0.8	0.3	1.7
σ		0.08	0.6	0.25	1.2	0.15	0.5	0.2	0.7	0.2	0.2	0.07	0.8	0.04	0.3	0.6	0.3
Ours	e_A	0.151	0.658	0.587	0.593	0.321	0.529	0.308	0.458	0.284	0.222	0.340	0.454	0.190	0.526	0.543	0.296
	e_S	0.128	1.053	0.663	0.442	0.441	0.557	0.441	1.667	0.434	0.258	0.395	0.827	0.312	0.468	0.503	0.446
	#f	40	34	31	38	119	23	34	27	96	66	108	25	73	44	22	79
KSR	e_A	0.231	0.951	0.605	0.372	0.454	0.557	0.401	0.560	0.350	0.247	0.423	0.491	0.257	0.677	0.553	0.381
	e_S	0.179	1.522	0.735	0.344	0.540	0.580	0.471	1.681	0.498	0.281	0.480	0.726	0.382	0.603	0.538	0.481
	#f	38	29	23	34	111	23	28	25	95	63	92	25	73	46	26	95
Polyfit	e_A	-	1.347	2.097	0.461	-	1.447	1.491	6.385	0.388	0.221	0.460	3.977	0.361	0.590	0.680	0.548
	e_S	-	1.170	1.385	0.343	-	1.089	1.259	3.325	0.500	0.297	0.537	2.592	0.524	0.556	0.572	0.683
	#f	-	14	25	30	-	16	18	17	150	63	98	26	144	51	19	90
Chauve	e_A	1.042	9.585	2.626	0.407	0.545	1.422	1.429	3.931	0.328	0.207	0.462	0.421	0.357	0.790	0.526	0.459
	e_S	0.772	5.172	1.704	0.308	0.555	1.082	0.823	2.137	0.407	0.261	0.488	1.195	0.411	0.671	0.465	0.911
	#f	25	32	103	56	261	25	18	14	528	107	188	36	202	125	54	700
SP_QEM	e_A	2.815	4.081	6.344	2.873	1.435	4.287	2.373	2.922	0.722	2.969	0.724	2.814	2.124	2.847	2.871	2.127
	e_S	1.575	2.482	3.856	1.934	1.069	3.000	1.513	1.971	0.756	1.933	0.777	1.831	1.509	1.984	1.645	1.498
	#f	39	28	22	26	110	24	27	25	100	62	92	25	72	46	26	92
SP_VSA	e_A	0.752	4.222	2.673	1.593	1.002	1.906	1.181	1.762	1.724	1.404	1.058	2.894	1.201	2.066	0.911	0.894
	e_S	0.538	3.107	1.921	1.316	1.031	1.664	0.958	1.806	1.287	0.960	0.918	2.355	1.091	1.422	0.704	0.806
	#f	717	213	157	947	175	420	528	113	93	682	127	31	83	568	123	270
SP_SAMD-CP	e_A	1.164	1.138	0.806	0.387	1.042	1.797	1.341	1.965	0.366	2.363	0.745	0.842	0.907	0.704	0.760	1.361
	e_S	0.675	0.988	0.781	0.307	0.909	1.302	0.833	1.556	0.383	1.480	0.789	0.761	0.744	0.604	0.552	0.998
	#f	141	95	92	267	162	40	75	35	352	105	120	102	137	125	98	125
SP_SAMD	e_A	1.428	1.524	1.071	1.885	0.585	2.326	0.801	1.483	0.657	1.546	0.508	1.686	0.800	1.240	1.907	0.686
	e_S	0.902	1.059	1.240	1.359	0.820	1.394	0.776	1.840	0.907	1.481	0.806	1.721	0.971	0.940	1.186	0.766
	#f	39	28	23	32	112	21	29	26	96	64	92	25	72	46	26	93

Table 5. Quantitative comparisons on the simple models of the KSR42 dataset. Types of objects include urban (U), freeform (F), indoor (I) and structured (S). Origins of point cloud include multiview stereo (MVS), laser scanning (Laser) and point sampled from CAD models (CAD). The size of input points #pts ranges from 101K to 1.2M points. The fitting tolerance ϵ and the minimal primitive size σ are expressed in percent of the bounding box diagonal and in percent of the total number of input points respectively. The evaluation metrics e_S, e_A, #f refer to the symmetric mean Hausdorff error (in % of the bounding box diagonal), the mean Hausdorff error from input points to output model and the number of output facets respectively. Note that the scalability of Polyfit is too low to return a result on Barn MVS and Bunny after several hours of computing.

		Asian dragon	Castle	Church	Courthouse	Euler	Fertility-Fine	Full thing	Meeting Room	Navis	Tower of Pi
Type		F	U	I	U	I	F	S	I	I	F
Origin		Laser	CAD	Laser	Laser	Laser	Laser	CAD	Laser	Laser	CAD
# pts		3.6M	737K	31.1M	1.9M	2.7M	242K	1.4M	3.1M	3.6M	2.9M
ϵ		0.25	0.1	0.8	0.8	0.1	0.2	0.2	0.1	0.1	0.1
σ		0.004	0.001	0.005	0.002	0.004	0.03	0.004	0.003	0.005	0.001
Ours	e_A	0.057	0.002	0.372	0.088	0.057	0.046	0.060	0.197	0.055	0.013
	e_S	0.064	0.033	0.239	0.136	0.094	0.086	0.062	0.146	0.048	0.031
	#f	3210	748	387	2157	1118	831	1788	1449	546	12749
KSR	e_A	0.065	0.006	0.460	0.134	0.069	0.061	0.064	0.198	0.061	0.020
	e_S	0.069	0.038	0.292	0.183	0.108	0.095	0.064	0.146	0.057	0.039
	#f	3132	711	394	1795	1317	998	1807	1491	457	12059
SP_QEM	e_A	0.071	0.044	0.292	0.155	0.148	0.082	0.170	0.299	0.167	0.135
	e_S	0.072	0.082	0.345	0.245	0.237	0.117	0.141	0.204	0.146	0.098
	#f	3132	712	394	1795	1318	1000	1806	1490	458	12050
SP_VSA	e_A	0.125	0.098	0.569	0.254	0.242	0.183	0.378	0.202	0.192	0.295
	e_S	0.108	0.110	0.377	0.262	0.240	0.243	0.245	0.160	0.164	0.241
	#f	3351	1894	494	1818	4070	982	4368	4949	522	27285
SP_SAMD-CP	e_A	0.114	0.065	0.187	0.154	0.169	0.150	0.117	0.330	0.098	0.104
	e_S	0.101	0.078	0.214	0.195	0.166	0.152	0.094	0.215	0.079	0.110
	#f	3672	1600	1924	1835	1450	1709	10046	1552	1898	30654
SP_SAMD	e_A	0.088	0.073	0.238	0.113	0.128	0.128	0.371	0.185	0.113	0.194
	e_S	0.094	0.095	0.274	0.223	0.199	0.163	0.258	0.168	0.114	0.205
	#f	3132	733	396	1800	1318	999	1809	1491	457	12060

Table 6. Quantitative results on advanced models. Note that Polyfit [6]and Chauve's algorithm [2] do not scale well enough to produce results on advanced models.

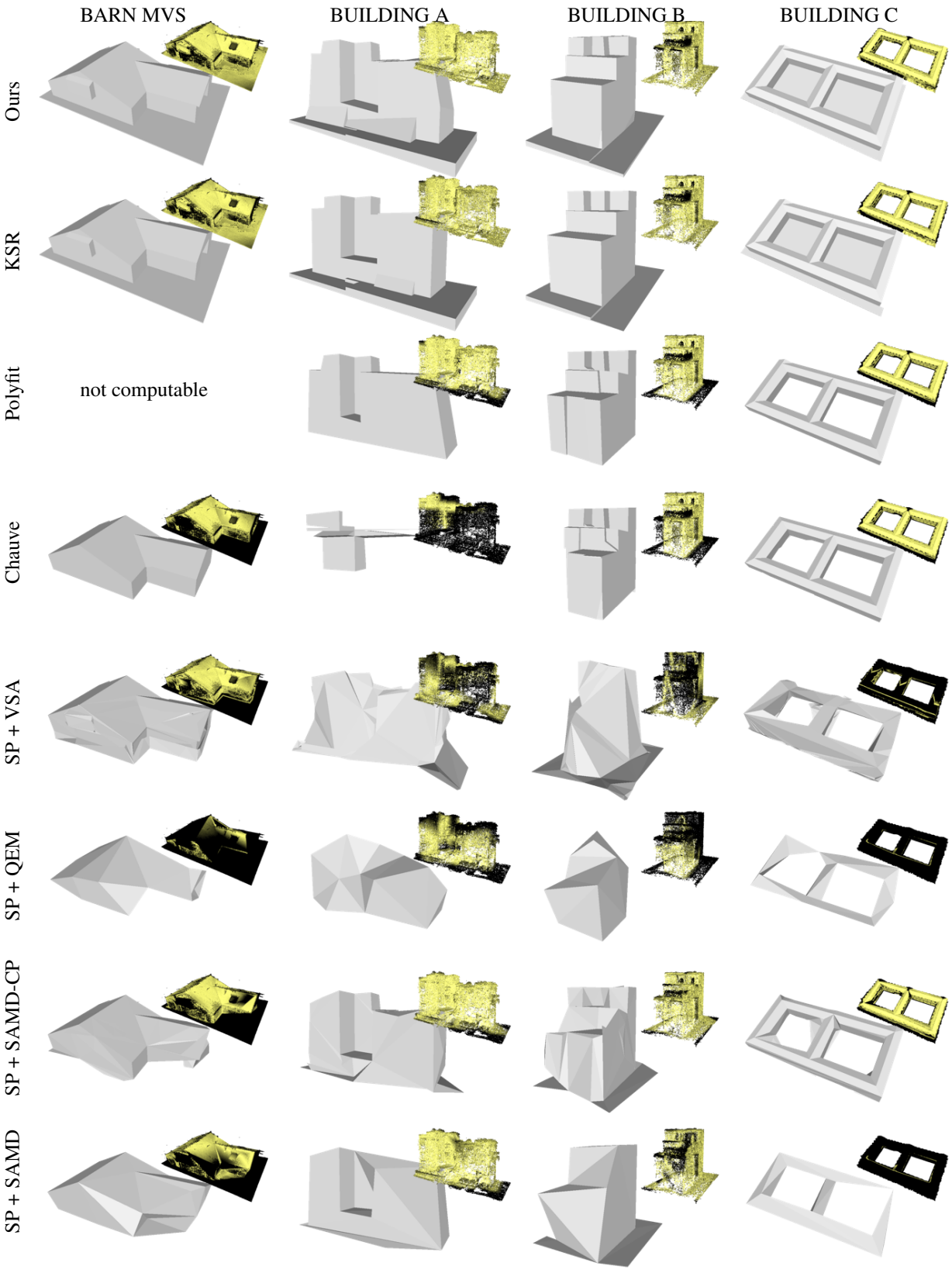

Figure 3. Visual comparisons on simple models (part 1/4). The colored point clouds correspond to the distribution of the Hausdorff distance from input points to output models (yellow=0, black$\geq \epsilon$). Evaluation scores associated with these results are given in Table 5.

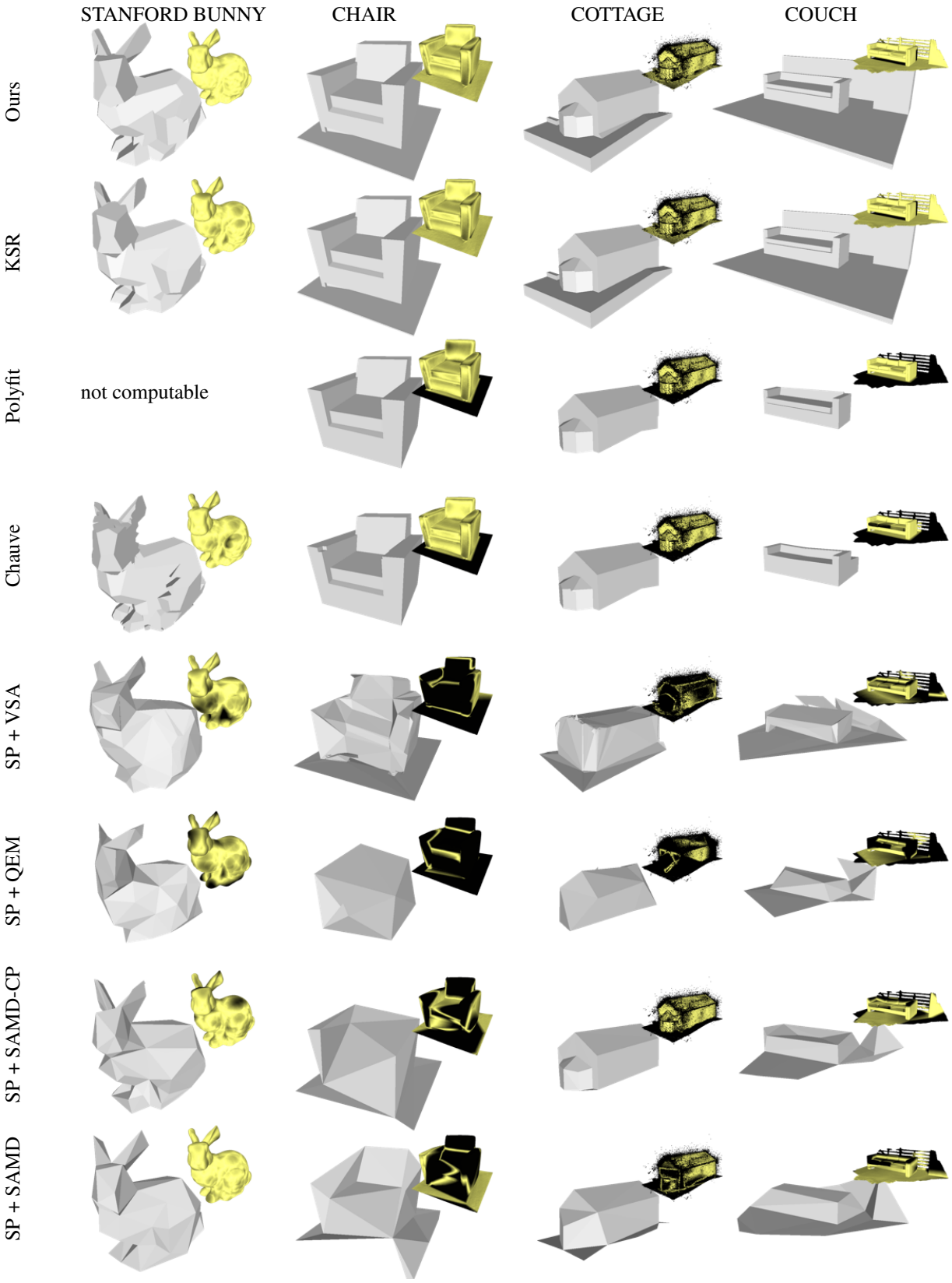

Figure 4. Visual comparisons on simple models (part 2/4).

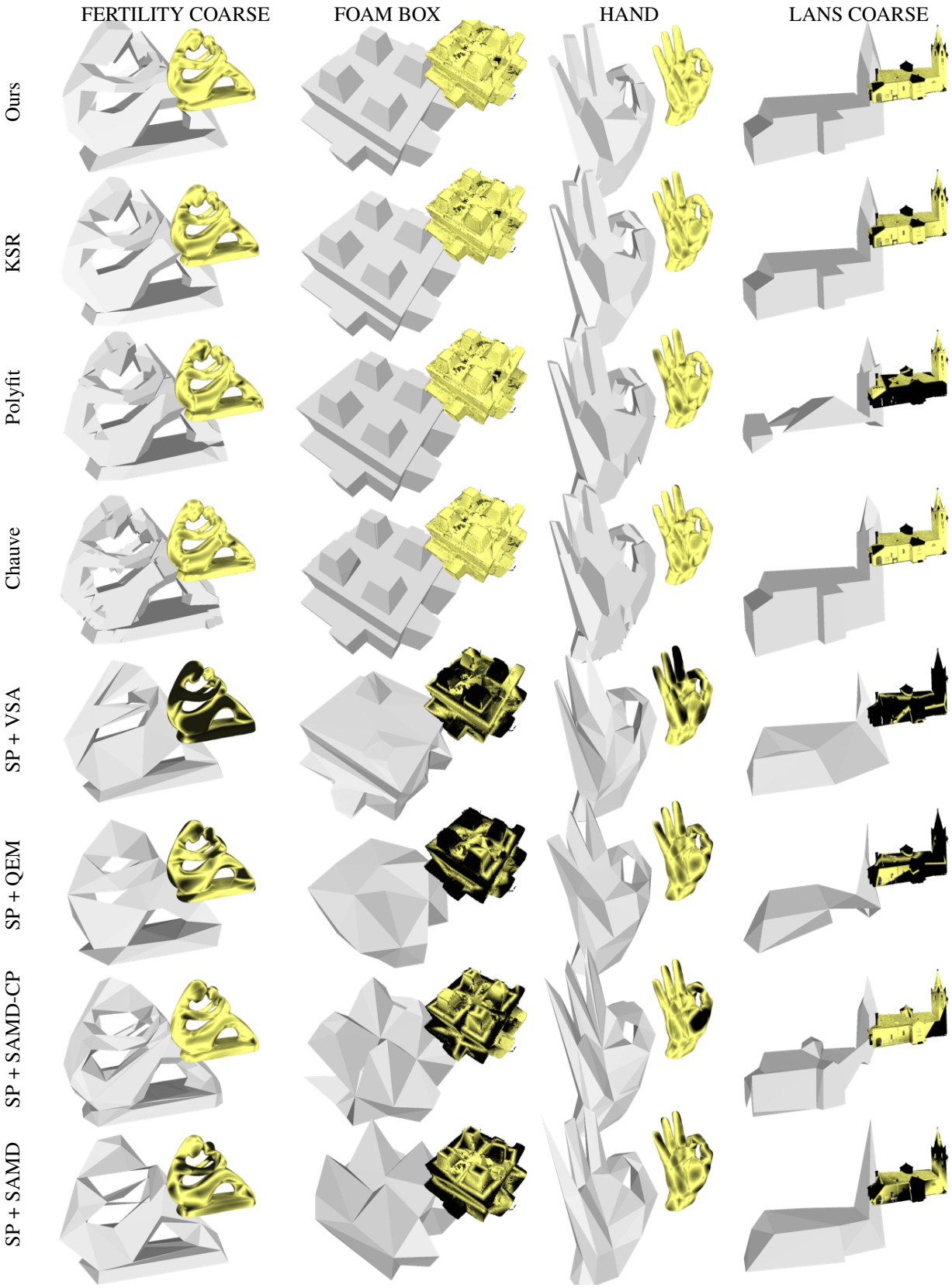

Figure 5. Visual comparisons on simple models (part 3/4).

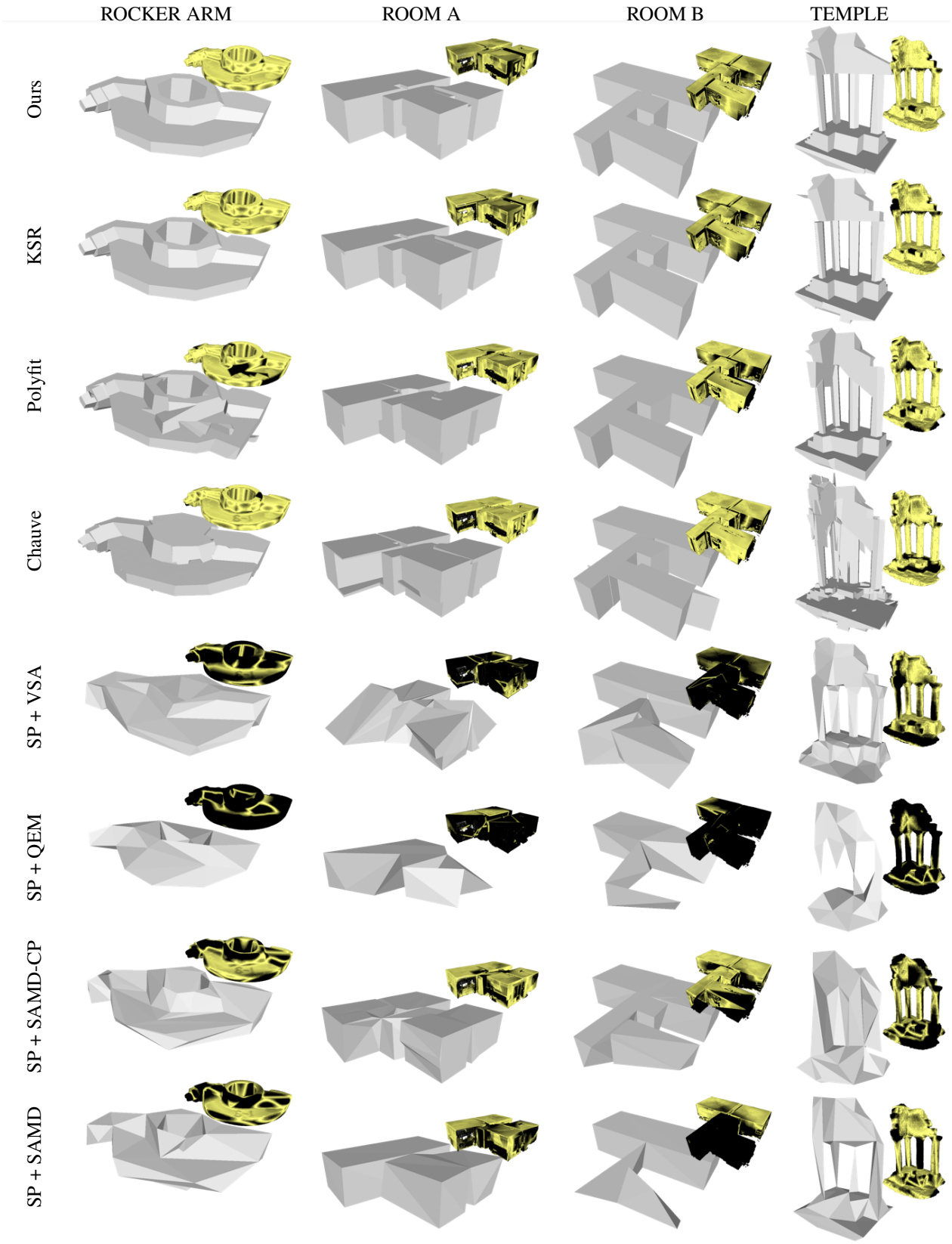

Figure 6. Visual comparisons on simple models (part 4/4).

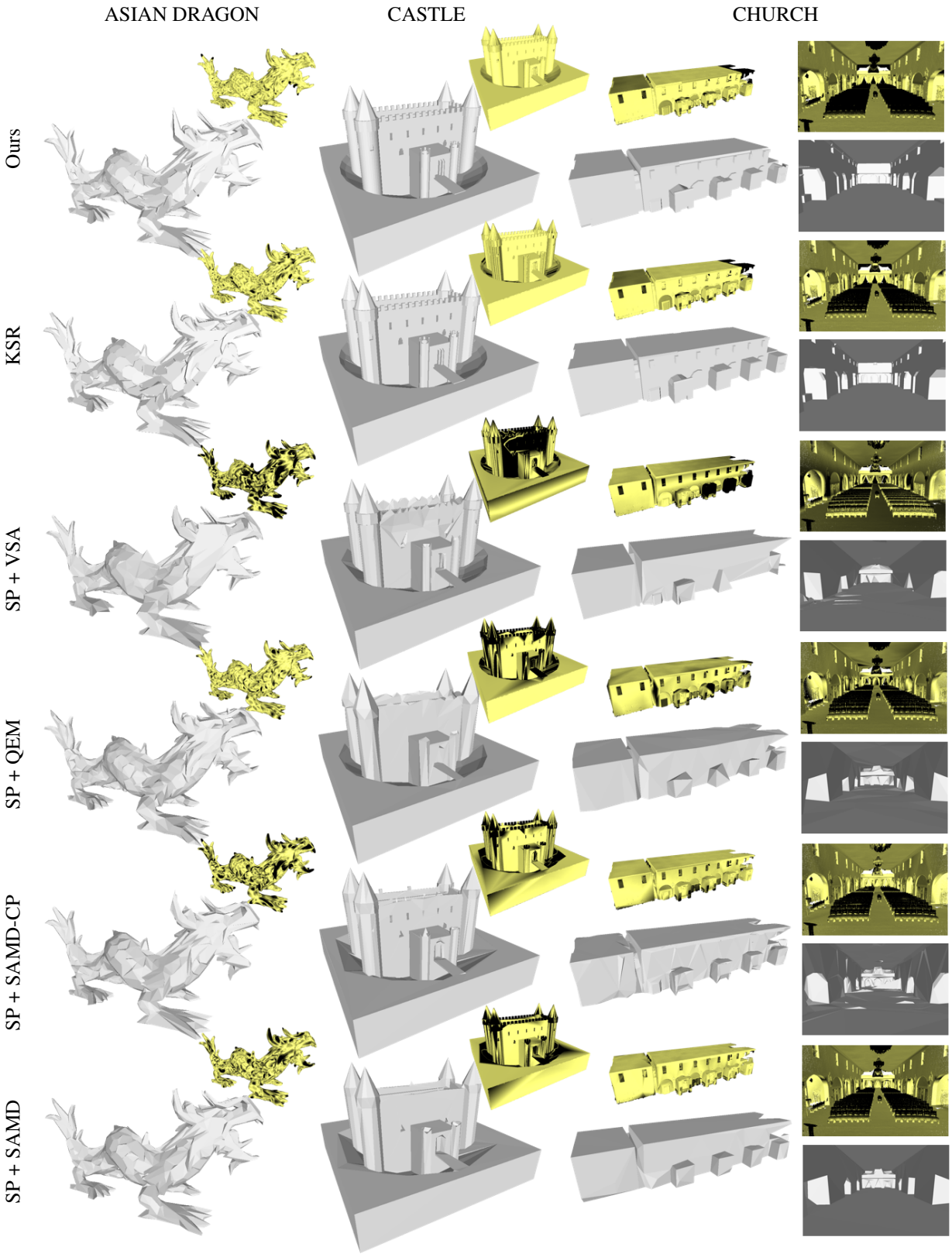

Figure 7. Visual comparisons on advanced models (part 1/4). Evaluation scores associated with these results are given in Table 6.

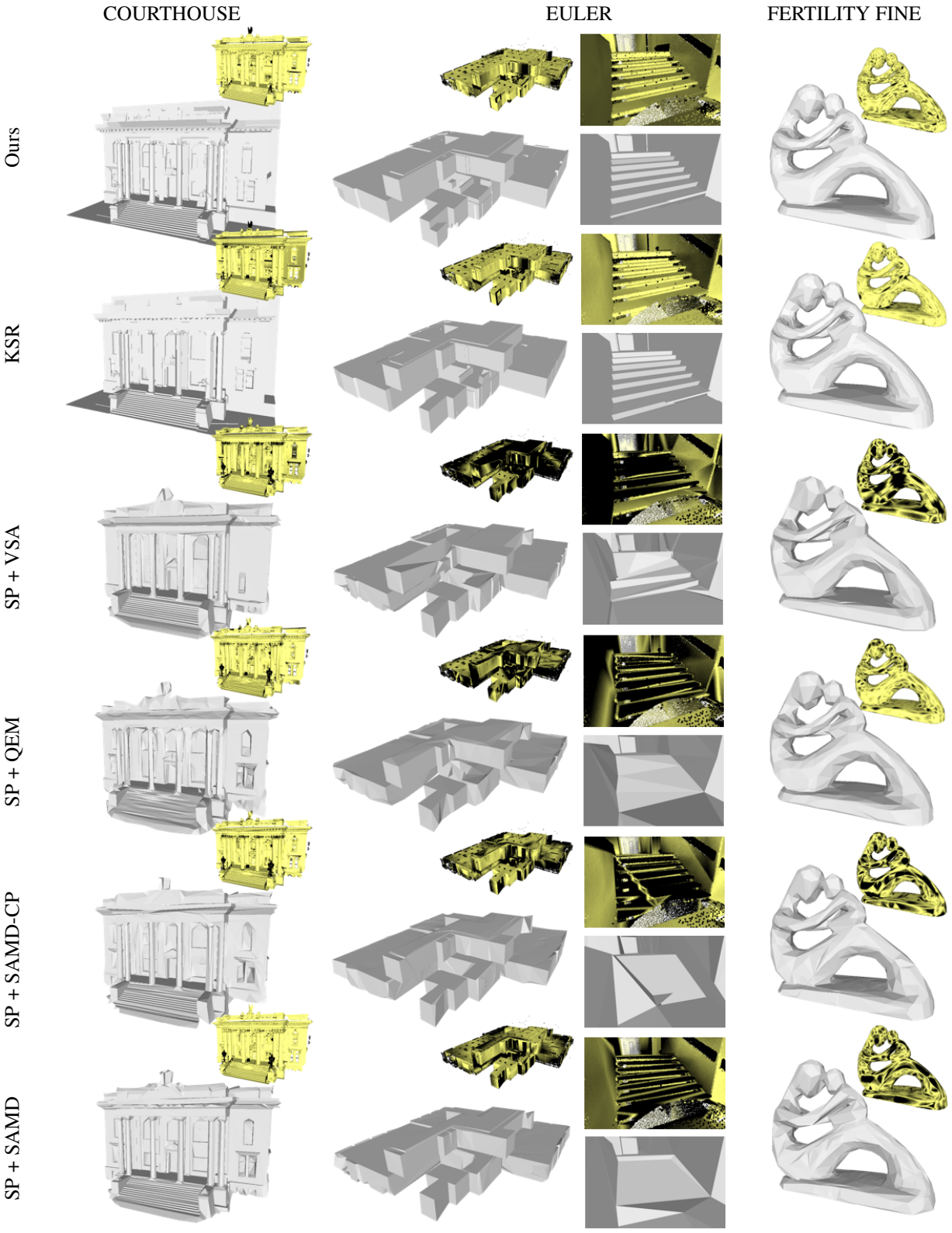

Figure 8. Visual comparisons comparisons on advanced models (part 2/4).

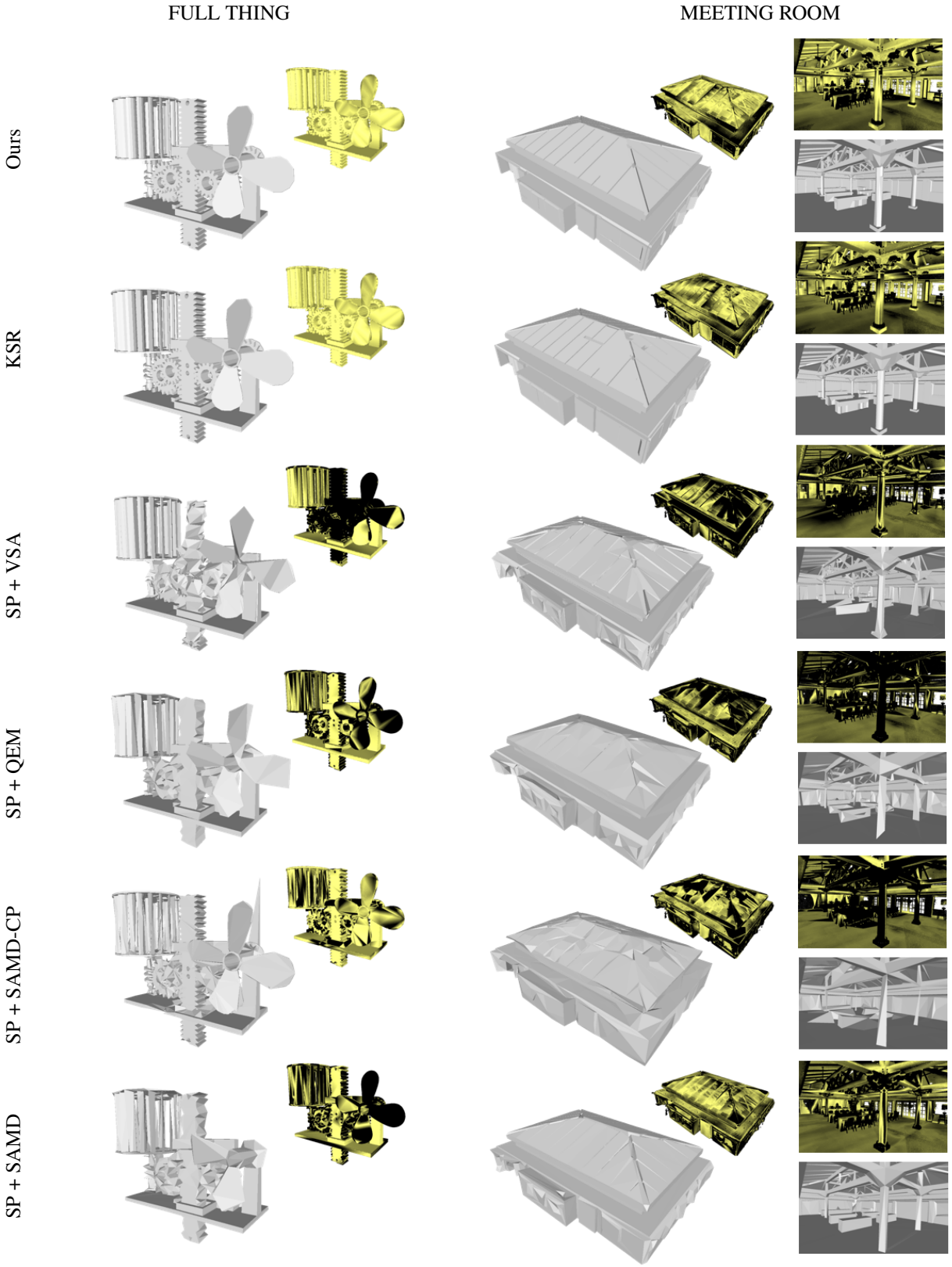

Figure 9. Visual comparisons on advanced models (part 3/4).

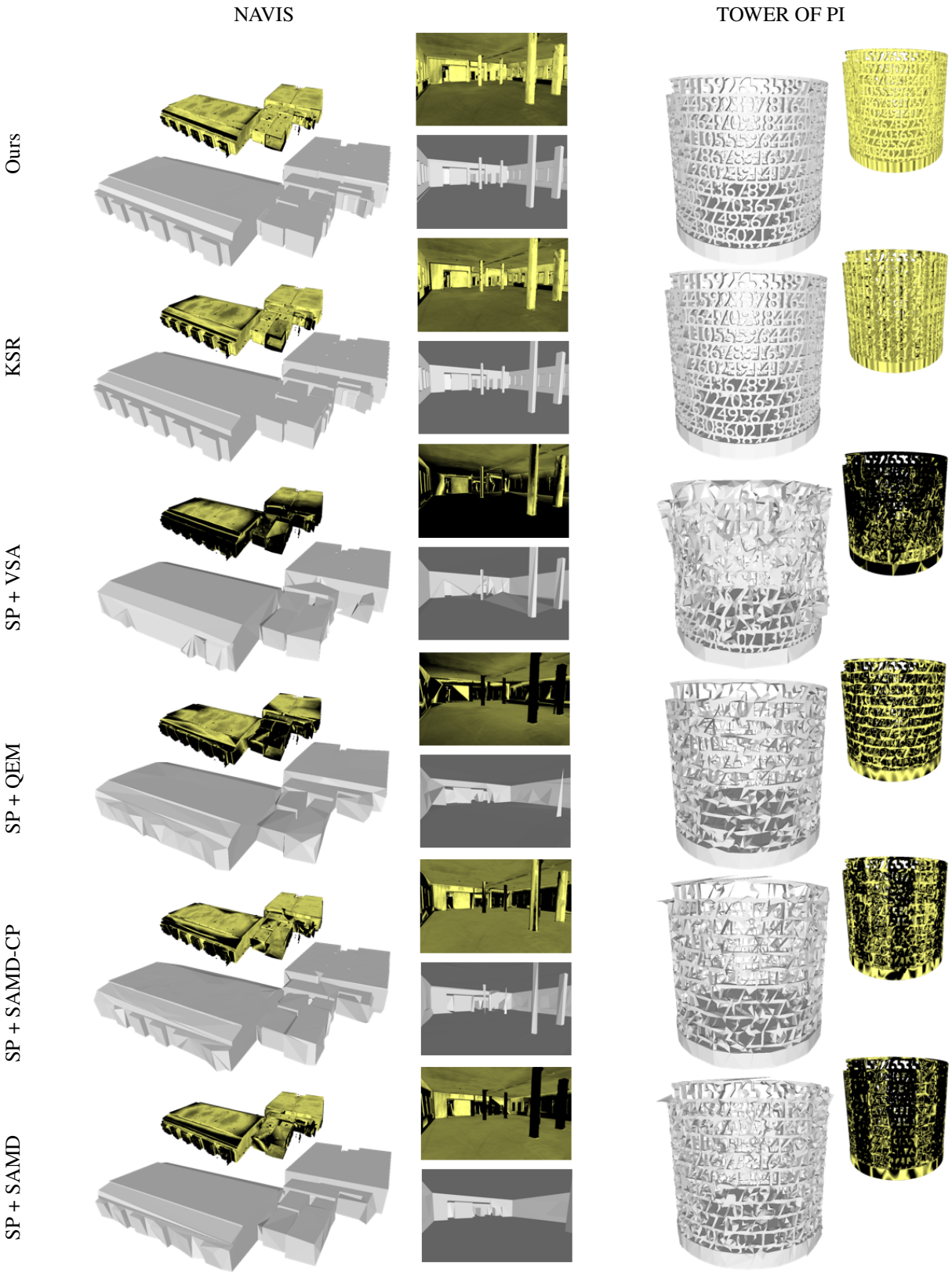

Figure 10. Visual comparisons on advanced models (part 4/4).